



OPEN

SUBJECT AREAS:
OPTICAL MATERIALS AND
STRUCTURES
ELECTRONIC STRUCTUREReceived
19 December 2014Accepted
5 March 2015Published
30 March 2015Correspondence and
requests for materials
should be addressed to
J.Z. (zjy@buaa.edu.cn)

Tuning oxygen vacancy photoluminescence in monoclinic Y_2WO_6 by selectively occupying yttrium sites using lanthanum

Bangfu Ding¹, Chao Han¹, Lirong Zheng², Junying Zhang¹, Rongming Wang³ & Zilong Tang⁴

¹Key Laboratory of Micro-nano Measurement, Manipulation and Physics (Ministry of Education), Department of Physics, Beihang University, Beijing 100191, China, ²Beijing Synchrotron Radiation Facility, Institute of High Energy Physics, Chinese Academy of Sciences, Beijing 100049, China, ³School of Mathematics and Physics, University of Science and Technology Beijing, Beijing 100083, China, ⁴State Key Laboratory of New Ceramic and Fine Processing, Tsinghua University, Beijing 100084, China.

The effect of isovalent lanthanum (La) doping on the monoclinic Y_2WO_6 photoluminescence was studied. Introducing the non-activated La^{3+} into Y_2WO_6 brings new excitation bands from violet to visible regions and strong near-infrared emission, while the bands position and intensity depend on the doping concentration. It is interesting to find that doping La^{3+} into Y_2WO_6 promotes the oxygen vacancy formation according to the first-principle calculation, Raman spectrum, and synchrotron radiation analysis. Through the Rietveld refinement and X-ray photoelectron spectroscopy results, La^{3+} is found to mainly occupy the Y2 (2f) site in low-concentration doped samples. With increasing doping concentration, the La^{3+} occupation number at the Y3 (4g) site increases faster than those at the Y1 (2e) and Y2 (2f) sites. When La^{3+} occupies different Y sites, the localized energy states caused by the oxygen vacancy pair change their position in the forbidden band, inducing the variation of the excitation and emission bands. This research proposes a feasible method to tune the oxygen vacancy emission, eliminating the challenge of precisely controlling the calcination atmosphere.

Tungstates are a kind of self-activated luminescence materials. That can be divided into several categories, normal metal tungstates (MWO_4), rare earth tungstates (Re_2WO_6) and poly-tungstates^{1–3}. Since Kroger concluded that the lattice group (WO_4^{2-}/WO_6^{6-}) itself was responsible for the luminescence origin⁴, what influenced tungstates luminescence properties was explored extensively such as morphology, size and dimension^{5,6}. In addition to intrinsic emission of anion-cation groups, there was also emission from defect states, inevitably incurred because of the abundant synthesis methods and flexible annealing temperatures and atmospheres^{7–9}. For example, the photoluminescence intensity of amorphous $BaWO_4$ was higher than that of crystalline $BaWO_4$ because of different annealing temperatures¹⁰. Therefore, the tungstate hosts luminescent properties were of great interest^{11,12}.

Though various methods have been employed to improve luminescent properties, process parameters especially annealing atmospheres, in particular oxygen partial pressure, were not controlled precisely¹³. An easy and convenient approach is to dope impurities in matrixes to enhance emission or obtain multi-color emission^{14–16}. The impurity can be any elements for the non-isovalent doping, such as trivalent rare earth and monovalent alkaline metal ions^{17,18}. This method has been extensively investigated in luminescent compounds, photocatalysts, and magnetic materials. For example, La^{3+} -doped ZnO has high photocatalytic activity¹⁹, and $LaCoMnO_6$ presents the coexistence of ferromagnetic and antiferromagnetic properties with increased Ca^{2+} substitution amounts²⁰. For tungstates, this approach mainly aims at enhancing luminescent intensity, changing optical activity, or broadening emission wavelength range^{21–23}. For instance, the emission wavelength of $CaW(Mo)O_4$ nanoparticles was tuned from blue-green or yellow to white by increasing the Dy^{3+} concentration²⁴. In addition, there are considerable reports on the La^{3+} doping effect on the luminescence properties of $PbWO_4$ ^{25,26}. According to the first principles study, different electronic compensation effects lead to different defect states in the band gap for high and low doping conditions, which explains the 420 nm band origin and new red absorption band²⁷.



Similarly, the isovalent doping can also change the luminescence properties of matrixes such as salt compounds and oxides^{28,29}. White up-conversion luminescence and enhanced emission were obtained in Yb³⁺/Er³⁺/Tm³⁺ doped YAlO₃ and Ca²⁺-doped MgO nanocrystals. The isovalent doping technique is often considered in tungstates, especially rare earth tungstates. The energy transfer processes of rare earth tungstates doped with Eu³⁺, Sm³⁺, Dy³⁺ and co-doped with Eu³⁺/Tb³⁺ have been summarized by Kaczmarek and Deum³⁰. However, the photoluminescence mechanism of the matrix such as lanthanum, lutetium and yttrium tungstates (La₂WO₆, Lu₂WO₆, Nd₂WO₆ and Y₂WO₆)^{31–37} after importing isovalent and non-activated ions is still open to be exploited. The luminescent properties of Bi₂WO₆ with and without La³⁺ doping were compared at low temperature 4 K³⁸, having found that La³⁺ doping increased the stokes shift of the matrix luminescence.

Various activators and sensitizers have been doped to improve the emission of monoclinic Y₂WO₆^{33–37,39}. The main purposes of these investigations are how to obtain white-light emission or promote energy conversion efficiency. The oxygen vacancy and local crystal structural regulation of monoclinic Y₂WO₆ by non-activated ions have not been reported until now. Recently, we⁴⁰ found that the atmosphere and calcination temperature induced the changes of oxygen vacancy concentration and tungsten coordination number in monoclinic Y₂WO₆, and thus affected the appearance of long-wave excitation and near-infrared emission bands. By calcining Y₂WO₆ in the air at 1200°C, the 340 nm excitation band, caused by low-concentration oxygen-vacancy, was substantially enhanced in comparison with those calcined at high temperature or in argon. Calcining in argon resulted in strong infrared emission because of the increased oxygen vacancy concentration⁴⁰. But the oxygen partial pressure, which depends on the airtightness of the furnace, cannot be controlled purposefully when the sample is calcined in the air. Therefore, it is ideal to tune the oxygen vacancy by a simple and feasible method on the basis of the doping approach advantages. Moreover, the mechanism behind the impurity effect on the luminescence of the matrix needs more intensive investigation to make up for the deficiency of the previous theory.

In this paper, a series of Y₂WO₆:xLa³⁺ (x = 0 and 0.01–0.05) powders are synthesized in air condition at 1250°C through the simple solid phase reaction. These samples show strong visible

emission. It is surprising to find that the 340 nm excitation intensity of the powders with dopant concentration not more than 3 at% is stronger than that of the pristine Y₂WO₆. The La³⁺ doping can also produce many new excitation bands in the ultraviolet and visible regions. These new excitation bands are ascribed to the different oxygen vacancy pair behavior induced by occupation variation of La³⁺ in the three Y sites. When La³⁺ enters into the Y2 (2f) site at low concentration, the oxygen vacancy pair energy band locates just above the valence band (VB), intensifying the 340 nm excitation band. At high doping concentration, the occupation number of La³⁺ in the Y3 (4g) site becomes high, bringing new localized energy states and excitation bands and weakening the 340 nm excitation intensity. The change of oxygen vacancy energy states generates different luminescence phenomenon.

Results and Discussion

Crystal structure. The crystal structure of pure Y₂WO₆ is monoclinic phase with space group 13-P₁₂/C₁-C_{2h}⁴ reported by Efremov⁴¹, whose inorganic crystal structure database (ICSD) number is 20955. In order to check the phase purity of as-prepared samples, X-ray diffraction (XRD) measurement results are plotted in Figure 1. All the XRD patterns agree well with the patterns of powder diffraction file (PDF) card 73-0118 and no peaks from other phases such as La₂WO₆ are observed. Due to the effective ion radius difference of Y³⁺ (0.96 Å and 1.019 Å for VII and VIII coordination) and La³⁺ (1.10 Å and 1.160 Å for VII and VIII coordination)⁴², the diffraction peaks of the La³⁺-doped samples slightly deviate when La³⁺ substitutes for Y³⁺.

The structure refinement of Y₂WO₆:xLa³⁺ (x = 0.03, 0.05) powders was performed through the general structure analysis system (GSAS) software package⁴³. The calculated patterns are consistent with the experimental XRD patterns (Supporting Information, Figure S1(a) and (b)). The atomic positions, occupation numbers, crystal structure and refinement parameters are listed in Table 1. The volumes of the samples gradually become larger with increasing La³⁺ content, while the atomic coordination and lattice parameters change a little. From the occupation numbers, one can see that La³⁺ enters into three Y sites simultaneously at any concentrations, occupying mainly the Y2 (2f) and Y3 (4g) sites and minorly the Y1 (2e) site. In 3.0 at% and 5.0 at% La³⁺-doped samples, the occupation

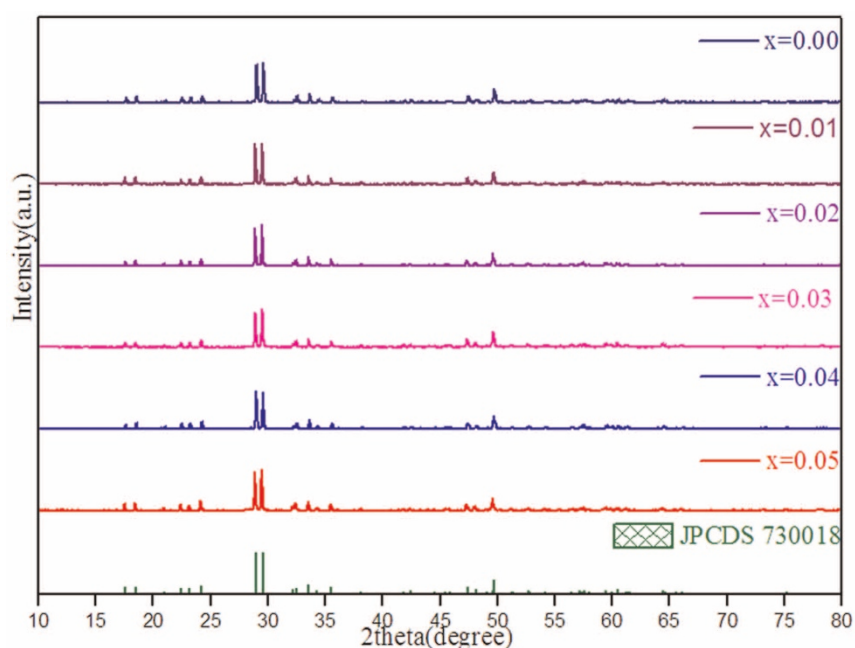


Figure 1 | XRD patterns of Y₂WO₆:xLa³⁺ (x = 0 and 0.01–0.05) powders calcined at 1250°C under air condition and PDF card 73-0018.



Table 1 | Atomic positions, occupation numbers, crystalline structure, and refined parameters of La³⁺-doped Y₂WO₆ samples. The crystal parameters of Y₂WO₆ are referenced in Ref. 41

Samples		Y ₂ WO ₆ :0.03La ³⁺				Y ₂ WO ₆ :0.05La ³⁺				Y ₂ WO ₆			
Atoms	Wyckoff	x	y	z	occupation	x	y	z	occupation	x	y	z	occupation
W	4g	0.27960	0.25318	0.38794	1.00	0.27867	0.2544	0.3879	1.00	0.2800	0.2524	0.3879	1.00
Y1	2e	0.00000	0.7360	0.25000	0.991	0.00000	0.7389	0.250000	0.99	0	0.7366	0.25	1.00
Y2	2f	0.50000	0.6857	0.25000	0.965	0.50000	0.6925	0.250000	0.948	0.5	0.6842	0.25	1.00
Y3	4g	0.20025	0.1916	0.07841	0.980	0.19905	0.1925	0.07849	0.956	0.1994	0.1921	0.0782	1.00
O1	4g	0.3602	0.1262	0.5658	1.00	0.3627	0.1054	0.5669	1.00	0.367	0.150	0.549	1.00
O2	4g	0.5297	0.3803	0.3853	1.00	0.5260	0.3907	0.3804	1.00	0.513	0.362	0.389	1.00
O3	4g	0.1586	0.5364	0.4268	1.00	0.1744	0.5497	0.4155	1.00	0.146	0.523	0.432	1.00
O4	4g	0.3045	-0.0344	0.2829	1.00	0.3047	-0.0293	0.2886	1.00	0.290	-0.012	0.272	1.00
O5	4g	0.0514	0.0332	0.4006	1.00	0.0579	0.0467	0.4040	1.00	0.065	0.036	0.396	1.00
O6	4g	0.2222	0.4791	0.21875	1.00	0.2342	0.4719	0.2246	1.00	0.216	0.463	0.232	1.00
La1	2e	0.00000	0.7360	0.25000	0.009	0.00000	0.7389	0.25000	0.01	-	-	-	-
La2	2f	0.50000	0.6857	0.250000	0.035	0.50000	0.6892	0.25000	0.052	-	-	-	-
La3	4g	0.20025	0.1916	0.07841	0.02	0.19905	0.1925	0.07849	0.044	-	-	-	-
a, b, c (Å)		7.54419	5.33856	11.3670		7.59811	5.34229	11.3767		7.589	5.334	11.354	
α, β, γ (°)		90	104.396	90		90	104.376	90		90	104.41	90	
V (Å ³)			446.386				447.337				445.15		
R _{wpr} , R _p , χ ²		10.22%	8.19%	6.598		12.31%	9.29%	8.416		-	-	-	

numbers of La³⁺ at Y1 (2e), Y2 (2f), and Y3 (4g) sites are 0.009, 0.035, and 0.02 and 0.01, 0.052 and 0.044, respectively. Hence, the occupation numbers of La³⁺ in the Y2 (2f) and Y3 (4g) sites gradually become higher with increasing La³⁺ concentration, and their variation quantities are 0.017 and 0.024, whereas, La³⁺ hardly enters into the Y1 (2e) site under this experimental condition.

There is a W (4g) site possessing C₁ symmetry, which is surrounded by six O atoms to form distorted octahedral coordination. The bond lengths of the six W-O are not identical each other. Three kinds of Y sites were coordinated with eight (2e, 2f) and seven (4g) oxygen atoms constructing polyhedron coordination. The Y1 (2e) and Y2 (2f) sites have C₂ symmetry, while the Y3 (4g) site takes on C₁ symmetry⁴⁴. The average Y-O bonds length is 2.3 Å for three Y sites. According to Pauling's electrostatic valence rule⁴⁵, the bond strengths (S) of yttrium and tungsten are $S_{Y1-O} = \frac{3}{8}$, $S_{Y2-O} = \frac{3}{8}$, $S_{Y3-O} = \frac{3}{7}$, and $S_{W-O} = \frac{3}{8}$. Thus the sum of ζ ($= \sum S_i = \frac{3}{8} + \frac{3}{8} + \frac{3}{7} + \frac{3}{8} = \frac{27}{14} \approx 1.93$) is approximately equal to the O²⁻ valence, indicating that Y₂WO₆ has stable structure. Because of isoelectrons between La³⁺ and Y³⁺, Y₂WO₆:xLa³⁺ also possesses a stable structure as evidenced by the invariability of the XRD patterns (Figure 1)⁴⁶⁻⁴⁹.

Photoluminescence properties. Figure 2 shows the photoluminescence (PL) emission and excitation spectra of all Y₂WO₆:xLa³⁺ (x = 0 and 0.01–0.05) samples. Under 340 nm excitation, the PL emission spectra have broad band shapes covering from 365 to 650 nm with maximal value around 470 nm. This band results from charge transition emission between the local oxygen 2p states (just above the VB) and the conduction band (CB)⁴⁰. The PL intensities in pure and low-concentration La³⁺-doped samples (x ≤ 0.03) are stronger than those of high-concentration La³⁺-doped powders. From Figure 2(a), the asymmetric shapes of emission spectra do not depend on dopant concentration and remain single-peak frameworks. In addition, the total, low-energy side, high-energy side half widths and peak values show slight dependence on La³⁺ concentration (Supporting Information, Table S1)⁵⁰. Thus, the emission band is composed of at least two overlapping bands⁵⁰.

Moreover, the powders also show the near-infrared emission in the scope of 1000–1700 nm as depicted in Figure 3(a)–(f). The pure sample displays strong luminescence in the 1300–1400 nm region

and weak emission in the 1450–1650 nm region. Under the 340, 378, 489, 512, 521, and 532 nm excitations, the 1–3 at% La³⁺-doped samples show strong emissions in two regions (1300–1400 nm and 1450–1650 nm). When the concentration continues to rise to 4 at% and 5 at%, the infrared luminescence is also observed in two regions (1300–1400 nm and 1450–1700 nm), besides much stronger emission from 1000 to 1150 nm. In order to exhibit the fine structure clearly, we have enlarged the emission spectra of 4 at% and 5 at% La³⁺-doped samples from 1300 nm to 1700 nm (supporting information, Figure S2). Tuning the La³⁺ content changes the infrared luminescence, suggesting the presence of ample local states in the band gap⁵¹.

To obtain a better understanding of photoluminescence phenomenon, Figure 2(b) displays the excitation spectra of all samples by monitoring 520 nm emission. All samples show three excitation bands containing two short wavelength bands (peaking at 280 and 310 nm) and one long wavelength band (peaking at 340 nm). When La³⁺ doping concentration increases from 1 at% to 3 at%, the 340 nm band gradually intensifies compared with the pristine sample. When the doping concentration exceeds 3 at%, the intensity of this band gradually weakens. A similar excitation band also appeared in other tungstates such as CaWO₄⁵² and ZnWO₄:Bi³⁺, Eu³⁺ phosphors⁵³. Their origins were ascribed to oxygen vacancy and ¹S₀ → ³P₁ transitions of Bi³⁺. For air-annealed Y₂WO₆ samples^{34,40}, this band was originated from low-concentration oxygen vacancy. Therefore, the dramatic variation of the 340 nm excitation band intensity undoubtedly originates from the oxygen vacancy defect and La³⁺ doping effect. The tunable defect emission intensity is obtained by changing the La³⁺ content. When the detector wavelength extends to the near-infrared ranges, many new excitation peaks, such as 380, 491, and 523 nm, appear in 1–3 at% La³⁺-doped powders. For samples doped with higher content of La³⁺, a series of peaks at 380, 482, 522, 533, 577, and 591 nm are observed. These new excitation bands were ascribed to the oxygen vacancy pair in Y₂WO₆⁴⁰. In the pristine sample, only the 340 nm excitation band is observed. Hence the behavior of oxygen vacancy changes a lot due to the incorporation of La³⁺ in Y₂WO₆.

Local crystal environments. In order to explore these new excitation bands origins and intensity variation of the 340 nm excitation band, we carried out Raman measurement to determine the local vibration structure of all the samples. According to group theory^{40,54}, Y₂WO₆ crystals have 3N = 3 × 36 = 108 distinct Raman and Infrared

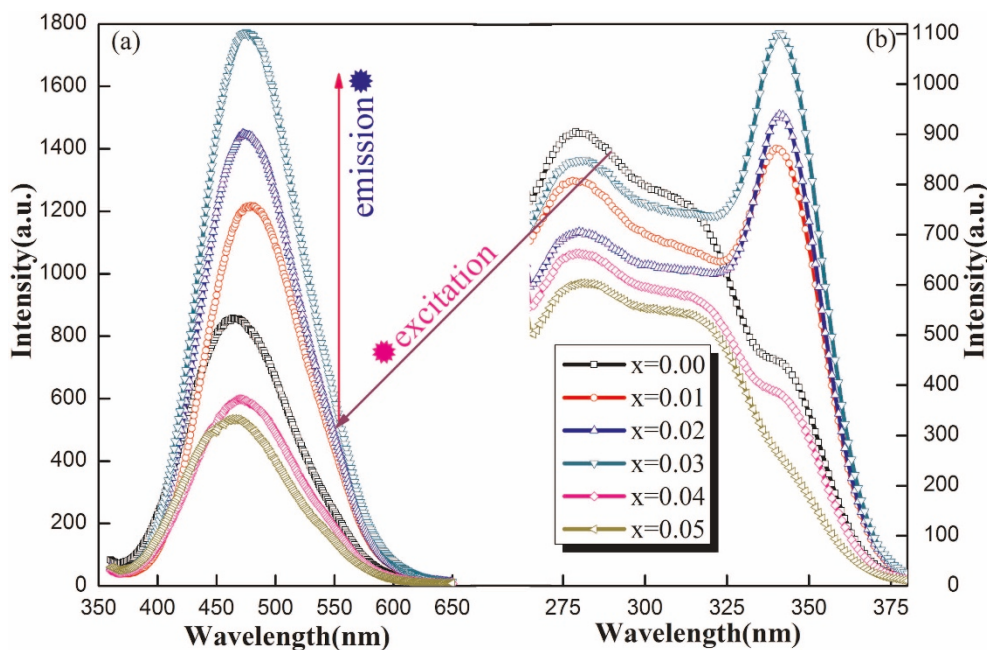


Figure 2 | PL emissions (a) and excitations (b) of $Y_2WO_6:xLa^{3+}$ ($x = 0$ and 0.01 – 0.05) powders calcined at $1250^\circ C$ in air.

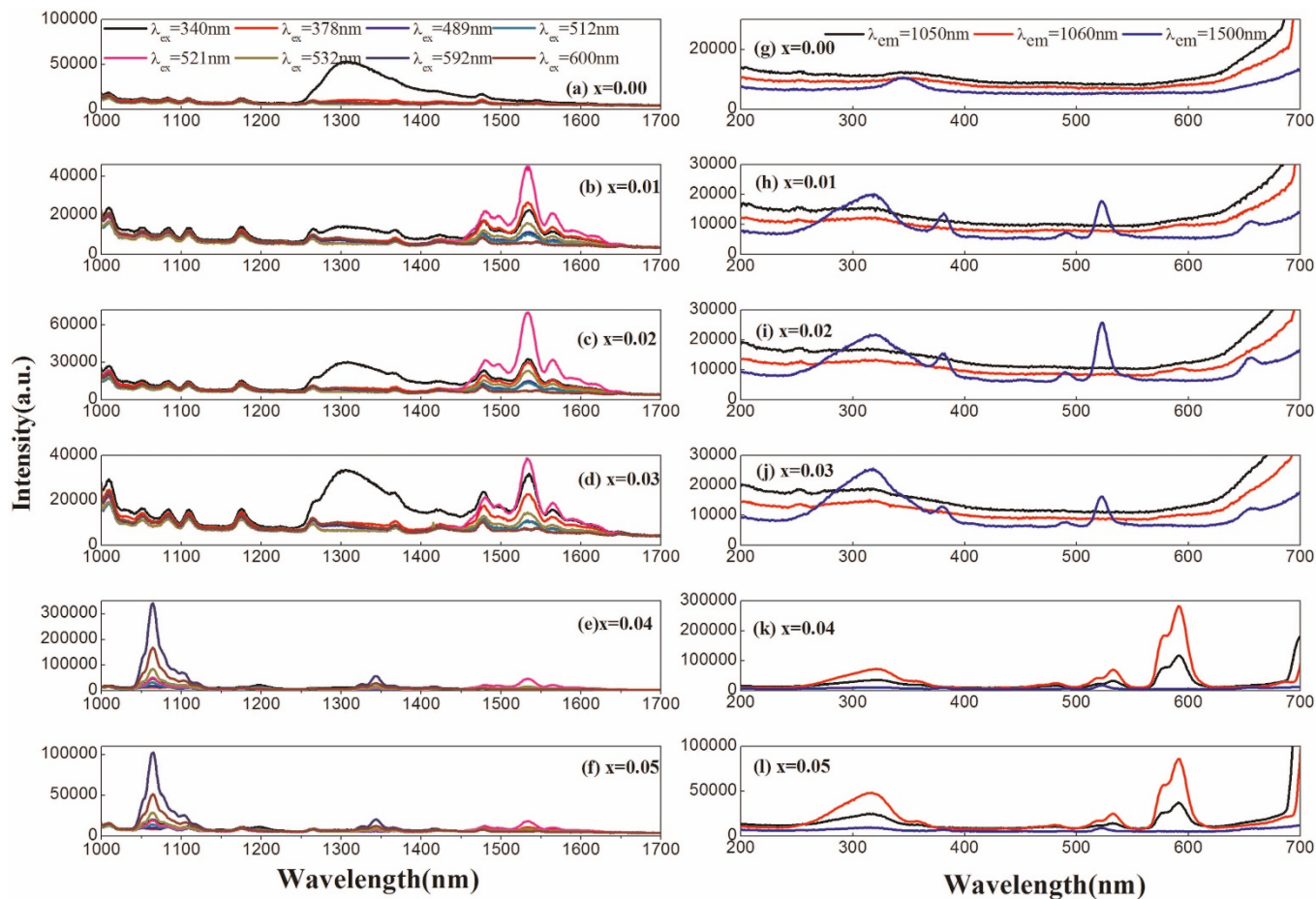


Figure 3 | (a)–(f) Emission spectra of $Y_2WO_6:xLa^{3+}$ phosphors burning in air conditions measured under different excitation wavelength. (g)–(l) Excitation spectra of $Y_2WO_6:xLa^{3+}$ powders measured by monitoring emission in the near-infrared region.



vibration modes. As we know, Raman spectra of tungstates can be identified with two types of groups as external and internal vibration modes⁵⁵. The external vibration modes concerning lattice phonons correspond to the motion of polyhedral $\text{YO}_{8/7}$ clusters. The internal vibration modes originates from the vibration of distorted octahedral WO_6 clusters^{56,57}, which are written as $\Gamma_{\text{internal vibration}} = A_{1g} + E_g + F_{2g} + 2F_{1u} + 2F_{2u}$.

The Raman active vibration modes of all $\text{Y}_2\text{WO}_6:\text{xLa}^{3+}$ powders ranging from 100 to 1000 cm^{-1} are shown in the Supporting Information (Figure S3). Table 2 lists all the Raman peaks positions and the coordination numbers according to similar chemical formulas $\text{M}_2\text{W}(\text{Mo})\text{O}_6$ ($\text{M} = \text{La}, \text{Nd}, \text{Sm}, \text{and Bi}$)⁵⁷. In the undoped sample, the strongest peak at 834 cm^{-1} is assigned to the $\text{W} = \text{O}$ symmetrical stretching vibration A_{1g} mode and has a half width of 20 cm^{-1} , which indicates that the coordination number (CN) between tungsten and oxygen is 6^{40,57}. The weak peaks at 707, 694, 668, 645, 621, 596, 550, 521, 501, 471, 446, 426, 394, 375, 365, 354, 340, 309, 290, 282, 270, 253, 238, 225, 215, 199, 192, 178, 142, 127, 118, and 104 cm^{-1} are internal vibration modes representing the tungsten CN being 6. Moreover, there are a small amount of five coordination tungsten atoms with the peaks position at 170 and 155 cm^{-1} . Compared with the previous results of Y_2WO_6 calcined in air⁴⁰, it is confirmed that the local crystal structure is sensitively affected by the calcination environment which depends on the individual furnace used during the samples preparation.

The Raman spectra of La^{3+} -doped samples differ from that of the pure sample by exhibiting some new Raman peaks. In $\text{Y}_2\text{WO}_6:\text{xLa}^{3+}$ ($x = 0.01\text{--}0.03$), the peaks at 798, 773, 381, and 207 cm^{-1} suggest that some tungsten atoms have tetrahedral coordination because the peaks positions are similar to those of La_2MoO_6 , Bi_2MoO_6 and Nd_2MoO_6 ⁵⁷. The peak value 156 cm^{-1} is analogous to that of Sm_2WO_6 , which indicates that CN of several tungsten atoms reduces to 5. Therefore, there exist tetrahedral and pentacoordinated tungsten atoms in 1–3 at% La^{3+} -doped samples. For high-concentration La^{3+} -doped samples, the peak shapes and numbers are almost similar to those of 1–3 at% La^{3+} -doped samples. In addition, the sudden enhanced peak at 934 cm^{-1} may be a combined tone with the sum of 773 and 156 cm^{-1} . Therefore, the tetra- and penta-fold tungsten atom numbers become larger after La ions are introduced into Y_2WO_6 . To study the crystal environments further, the extended

X-ray absorption fine structure (EXAFS) measurements of W-L_{III} absorption in $\text{Y}_2\text{WO}_6:\text{xLa}^{3+}$ ($x = 0$ and 0.01–0.05) samples are applied to determine the local structure around W atoms. Through Fourier transformation of the fine structure signals, Figure S4 shows the radical structure functions of W atoms. A strong peak in Figure S4 corresponds to the nearest neighbor O atoms of W ion. Furthermore, the fitting results are given in Table S2 by further Fourier fitting of this peak.

The average coordination number (CN) of tungsten and oxygen can be calculated as $\text{CN} = (\text{attenuation factor}) \times 6/A$, where A is the value of W-O in standard sample (generally 0.7–0.9) and 6 is the theoretical coordination number. From the table S2, the average number of tungsten is reduced with the increase of La^{3+} content. Hence, it is confirmed further that oxygen vacancy concentration becomes high gradually. Though the attenuation factor of 2 at% La^{3+} -doped sample is slightly larger than those of 1 at% and 3 at% La-doped samples, the three values are assumed approximately equal. The tungsten CN is gradually reduced with increasing La^{3+} concentration, which hints that oxygen vacancies exist in all samples. Since the external environments are the same in the experiment, the oxygen vacancy variation is undoubtedly ascribed to the doping effect of La^{3+} .

In order to shed more lights on the La^{3+} information in Y_2WO_6 , the XPS spectra of the La 3d core level for the $\text{Y}_2\text{WO}_6:\text{xLa}^{3+}$ with $x = 0.03$ and 0.05 are shown in Figure 4. The La 3d XPS in the two samples can be fitted as a superposition of four Gaussian components. The peaks at 834 and 851 eV can be attributed to two spin orbits of La 3d_{5/2} and La 3d_{3/2}, respectively⁵⁸. The other two peaks at 837 and 854 eV are La 3d satellite peaks. Hence, the double peak structure of each spin-orbit split agrees with the reported literatures⁵⁹. As we know, the split spin orbit reflects states with configurations $[3d^9]^{\text{hole}}4f^{\text{L}}$ and $[3d^9]^{\text{hole}}4f^{\text{L}}[\text{L}]^{\text{hole}}$, where L indicates the oxygen ligand. Generally, the f^{L} dominates the low binding energy signals, and the high binding energy is referred to the f^{I} peaks. Because the doping concentration has no obvious effect on the La 3d $f^{\text{I}}/f^{\text{L}}$ intensity ratio, the $f^{\text{I}}\text{--}f^{\text{L}}$ energy separation and peak shift are considered.

The $f^{\text{I}}\text{--}f^{\text{L}}$ separation values are 3.628 eV and 3.404 eV in these two samples, which differ from those in ABO_3 perovskites, La_2CuO_4 (3.1 eV), LaCoO_3 (4.3 eV) and $\text{La}_{1.85}\text{Ba}_{0.15}\text{CuO}_4$ (5.3 eV)⁵⁹. Thus,

Table 2 | The Raman peaks of all the samples and the corresponding coordination numbers (CN) are shown according to a similar formula $\text{M}_2\text{W}(\text{Mo})\text{O}_6$. The material in parentheses, such as La_2WO_6 , denotes that the Raman peak values equal to those in Ref. 57

No	Y_2WO_6	CN	$\text{Y}_2\text{WO}_6:\text{xLa}^{3+}$ ($x = 0.01\text{--}0.03$)	CN	$\text{Y}_2\text{WO}_6:\text{xLa}^{3+}$ ($x = 0.04, 0.05$)	CN	No	Y_2WO_6	CN	$\text{Y}_2\text{WO}_6:\text{xLa}^{3+}$ ($x = 0.01\text{--}0.03$)	CN	$\text{Y}_2\text{WO}_6:\text{xLa}^{3+}$ ($x = 0.04, 0.05$)	CN
1	-	-	934	-	934	-	22	340	6	340	6	340	6
2	834	6	834	6	834	6	23	309	6	309	6	309	6
3	-	-	798(La_2MoO_6)	4	-	-	24	290	6	290	6	290	6
4	-	-	773(La_2MoO_6)	4	773(La_2MoO_6)	4	25	282	6	282	6	282	6
5	707	6	714	6	707	6	26	270	6	270	6	270	6
6	694	6	694	6	694	6	27	253	6	253	6	253	6
7	668	6	668	6	668	6	28	238	6	238	6	238	6
8	645	6	645	6	645	6	29	225	6	225	6	225	6
9	621	6	621	6	621	6	30	215	6	215	6	215	6
10	596	6	596	6	596	6	31	-	-	207(Nd_2MoO_6)	4	207(Nd_2MoO_6)	4
11	550	6	550	6	550	6	32	199	6	199	6	199	6
12	521	6	521	6	521	6	33	192	6	189	6	189	6
13	501	6	501	6	501	6	34	178	6	178	6	178	6
14	471	6	466	6	466	6	35	170(Sm_2WO_6)	5	-	-	-	-
15	446	6	446	6	446	6	36	155(Sm_2WO_6)	5	156(Sm_2WO_6)	5	155(Sm_2WO_6)	5
16	426	6	426	6	426	6	37	142	6	142	6	142	6
17	394	6	394	6	394	6	38	127	6	127	6	127	6
18	-	-	381(Bi_2MoO_6)	4	381(Bi_2MoO_6)	4	39	118	6	118	6	118	6
19	375	6	-	-	-	-	40	-	-	113	6	-	-
20	364	6	362	6	362	6	41	104	6	104	6	104	6
21	354	6	354	6	354	6							

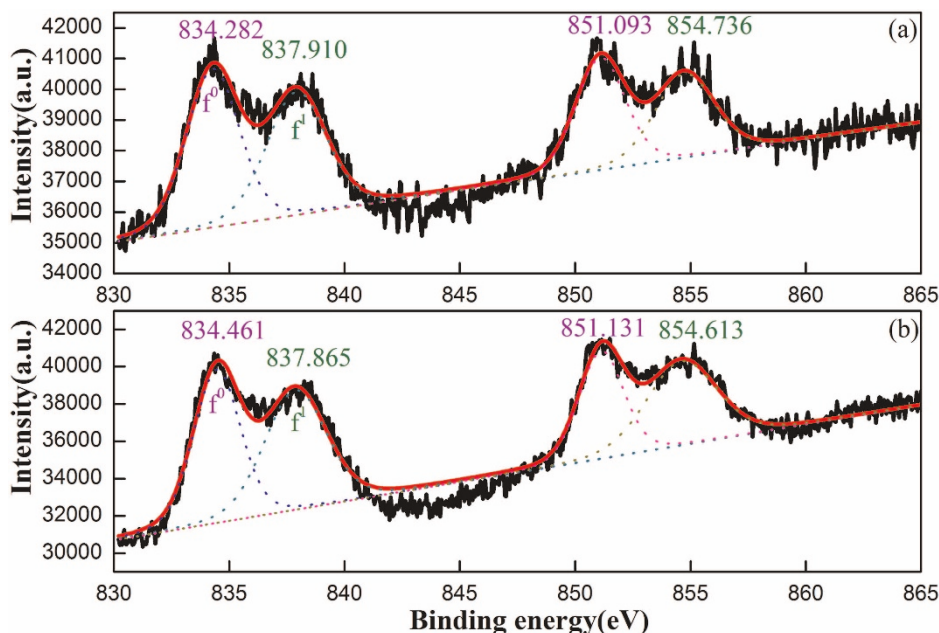


Figure 4 | XPS and their peak fitting curves of the La 3d region for the $Y_2WO_6:xLa^{3+}$ powders with $x = 0.03$ (a) and $x = 0.05$ (b).

the equivalent doping can change the f^1 - f^0 energy separation value, which is similar to that reported in the literature (3.6 eV for La^{3+} -doped ZnO)⁶⁰. Moreover, the La $3d_{5/2}$ and La $3d_{3/2}$ peaks shift to higher energy by 0.179 eV and 0.038 eV, and the satellite peaks shift to lower energy by 0.045 eV and 0.113 eV from $x = 0.03$ to $x = 0.05$ samples. These shifts really reflect the change in chemical potential. Different peak positions and f^1 - f^0 energy separation values reflect different contents of La in the three Y sites⁶¹, which agrees with Retveld refinement results. The La $3d_{5/2}$ and La $3d_{3/2}$ splitting distances for the $x = 0.03$ and $x = 0.05$ samples are estimated to be 16.81 and 16.670 eV, respectively, which further confirms that the occupancy site variation of La with its concentration induces the chemical state change.

Photoluminescence mechanism. To obtain the deep understanding of luminescence origin, the first principle method is often applied to derive electronic structures of luminescent materials⁶². The appearance of four- and five-coordination tungsten atom numbers from the pure to different-concentration La^{3+} -doped samples indicates that the oxygen vacancy concentration increases gradually with incorporation of La^{3+} into the samples. Hence, we first establish a perfect $1 \times 2 \times 1$ Y_2WO_6 supercell, and then one or two oxygen atoms next to tungsten are removed to constitute single and twin oxygen vacancies together with replacing the nearest Y atom with a La atom (these models are labeled as $La_{Yk} + V_{O(i)}$ and $La_{Yk} + V_{O(ij)}$ with $k = 1, 2, \text{ and } 3$ and $i, j = 1, 2, 3, 4, 5, \text{ and } 6, i \neq j$). Under oxygen-rich atmosphere, the defect formation energies ($E_{formation}$) of various models when oxygen vacancy locates at different sites are plotted in Figure 5. As illustrated in Figure 5(a), for the models containing one oxygen vacancy, the variation rules of $E_{formation}$ are the same for the undoped and La^{3+} -doped models expect for the model with $V_{O(6)}$. Their average values are calculated as 2.1593, 2.2175, 2.0334, and 2.2521 eV for pure and La^{3+} -doped models when La substitutes for Y at three sites. Comparing these two average $E_{formation}$ for $V_{O(i)}$ and $La_{Y2} + V_{O(i)}$ models, it can be found that when La^{3+} replaces Y2, the formation energy is reduced. This indicates that La^{3+} enters into the Y2 site most easily, and doping La^{3+} into Y_2WO_6 can really promote the formation of oxygen vacancies.

Though the average $E_{formation}$ for $V_{O(i)}$ is smaller than those of $La_{Y1} + V_{O(i)}$ and $La_{Y3} + V_{O(i)}$, La^{3+} also can occupy Y1 and Y3 sites

in the process of high-temperature calcination. Therefore, the probability of La entering into the Y2 site exceeds that of entering into Y1 and Y3 sites. The calculation results accord well with those of XRD refinement. For the $La_{Yk} + V_{O(ij)}$ models, the minimal $E_{formation}$ is located at different sites for the four configurations ($V_{O(ij)}$ and $La_{Yk} + V_{O(ij)}$). The average values of the four cases are 4.1819, 4.3838, 3.6547, and 4.4581 eV. Similarly, the $E_{formation}$ average value of $La_{Y2} + V_{O(ij)}$ is smaller than that of the $V_{O(ij)}$, and the difference of average $E_{formation}$ between $V_{O(ij)}$ and $La_{Yk} + V_{O(ij)}$ ($k = 1$ and 3) samples is very small. Hence, the La^{3+} doping induces oxygen vacancy increase, which is consistent with the analysis of Raman spectra and synchrotron radiation.

For self-activated luminescent tungstates, the CB and VB are mainly composed of W 5d and O 2p states. Thus, the tungstate luminescence origin is intrinsic luminescence⁶². Moreover, luminescence caused by intrinsic defects such as oxygen vacancies or interstitial atoms also exists in tungstates^{63,64}. For our samples, there exists amply oxygen vacancy luminescence information. As previously reported, the origin of the 340 nm excitation band is ascribed to low-concentration oxygen vacancy namely some five coordination tungsten atoms⁴⁰. In samples containing La^{3+} , the oxygen vacancy concentration increases in comparison with the pristine Y_2WO_6 , resulting in some four and five-fold tungsten atoms.

Based on these results, we calculate the electronic structure of the samples containing both La^{3+} and an oxygen vacancy pair, to exploit the role of La doping on the behavior of the oxygen vacancy pair. As found previously⁴⁰, single oxygen vacancy accounts for the excitation bands shorter than 400 nm (340 nm), while oxygen vacancy pair causes a series of excitation bands from 380 to 600 nm. We only need to find out why in the low-concentration La^{3+} -doped sample which contains an oxygen vacancy pair like the high-concentration La^{3+} -doped samples the 340 nm excitation band dominates. La^{3+} prefers to enter into the Y2 site at low concentration and then enters into the Y3 site at high concentration. Therefore, we studied the electronic structures of samples containing an oxygen vacancy pair, where La^{3+} occupies three Y sites, namely La_{Y1} , La_{Y2} , and La_{Y3} , respectively. When the $E_{formation}$ of these structures are closest to the average value of $E_{formation}$ in $La_{Yk} + V_{O(ij)}$, we calculated their electronic properties.

On the basis of the Y_2WO_6 crystal structure⁶⁵, three-type Y sites are surrounded by different kinds of oxygen atoms. The nearest

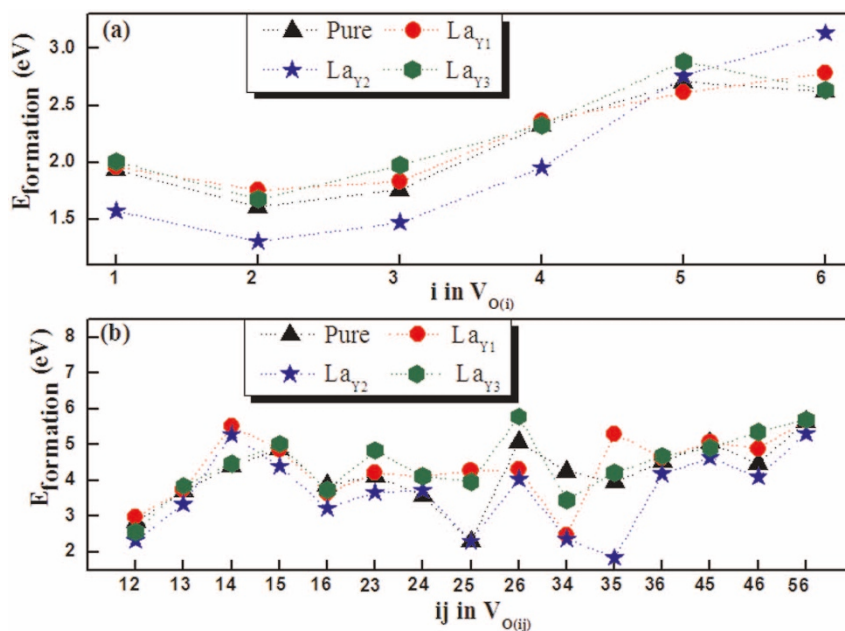


Figure 5 | The defect formation energies of (a) $V_{O(i)}$, $V_{O(i)} + La_{Yk}$ ($k = 1, 2,$ and 3) and (b) $V_{O(ij)}$, $V_{O(ij)} + La_{Yk}$ in oxygen-rich conditions.

neighbors of the Y1 (2e) site are O3(2), O4(2), O5(2), and O6(2) (the numbers in parentheses represent oxygen atom numbers). Similarly, O1(2), O2(2), O4(2), and O6(2) surround the Y2 (2f) site, and O1(1), O2(1), O3(1), O4(1), O5(2) and O6(1) surround the Y3 (4g) site. When La enters the Y $_k$ site, the nearest oxygen atoms escape to form oxygen vacancy easily, and then the other oxygen atoms different from the nearest oxygen species escape. Hence, the average $E_{\text{formation}}$ can be calculated for the nearest oxygen vacancy in the $La_{Yk} + V_{O(ij)}$ models. These average values are 4.6778, 3.7884 and 4.4581 eV for $La_{Y1} + V_{O(ij)}$, $La_{Y2} + V_{O(ij)}$, and $La_{Y3} + V_{O(ij)}$, respectively. Therefore, the electronic structures of $La_{Y1} + V_{O(36)}$, $La_{Y2} + V_{O(24)}$, and $La_{Y3} + V_{O(14)}$ configurations are calculated, because their $E_{\text{formation}}$ are closest to the average $E_{\text{formation}}$.

Figure 6 displays the total density of states (DOS) and partial DOS of the constituted atoms. The CB and VB are mainly composed of W

5d and O 2p states with small contributions of Y 4d. The contributions of all the La electron states for VB and CB are almost zero. The W 5p, Y 4s, W 5s, La 6s, La 4d, Y 4p, O 2s, and La 5p are located below the VB from -45 eV to -10 eV. The electronic structure properties of Y_2WO_6 are similar to those of some tungstates and molybdates such as scheelite $CaWO_4$ and wolframite $ZnMoO_4$ ^{66,67}. Therefore, the luminescence origin of Y_2WO_6 is mainly ascribed to the charge transfer transition between W and O⁶⁸. Moreover, the local state positions and numbers for the $La_{Y2} + V_{O(24)}$ model are similar to those of Y_2WO_6 with low-concentration oxygen vacancy⁴⁰. For $La_{Y1} + V_{O(36)}$ and $La_{Y3} + V_{O(14)}$ models, these states resemble those of Y_2WO_6 with high-concentration oxygen vacancy⁴⁰. Thus, these differences of local states induce different excitation and emission phenomena. In low-concentration La^{3+} -doped samples, La mainly enters into the Y2 sites resulting in ample oxygen vacancy pair.

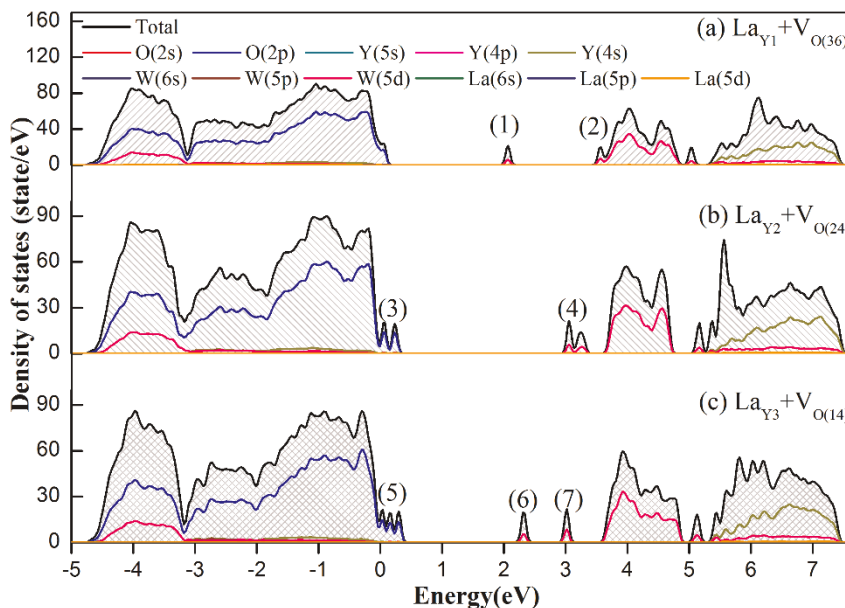


Figure 6 | The total and partial density of states of (a) $La_{Y1} + V_{O(36)}$ (b) $La_{Y2} + V_{O(24)}$ and (c) $La_{Y3} + V_{O(14)}$.



Table 3 | The k point (in the left of parentheses) and energy values (in the right of parentheses) of $\text{La}_{Y1} + \text{V}_{\text{O}(36)}$, $\text{La}_{Y2} + \text{V}_{\text{O}(24)}$ and $\text{La}_{Y3} + \text{V}_{\text{O}(14)}$ supercells. Max and Min refer to Maximum and Minimum

Models	VB	Local states	CB
$\text{La}_{Y1} + \text{V}_{\text{O}(36)}$	(0.5, 0.053) (Max)	(0, 2.03) (Min) (1.0, 3.51) (Min) (0.5, 3.64) (Min) (0, 3.725) (Min)	(0, 3.77) (Min)
$\text{La}_{Y2} + \text{V}_{\text{O}(24)}$	(0.5, -0.1) (Max)	(1.0, 0.017) (Max) (1.0, 0.18) (Max) (0, 3.025) (Min) (0, 3.286) (Min)	(0, 3.67) (Min)
$\text{La}_{Y3} + \text{V}_{\text{O}(14)}$	(0, -0.07) (Max)	(0, 0) (Max) (0, 0.15) (Max) (0.5, 0.27) (Max) (0, 2.27) (Min) (1.5, 3.0) (Min)	(1.5, 3.64) (Min)

When these samples are radiated under ultraviolet (UV) light larger than the gap value (E_{gap}) 3.75 eV, the electrons jump from the VB to the CB then relax and finally emit photons. Thus, the 280 nm and 310 nm excitation bands can be produced. When the UV light energy is smaller than E_{gap} , the electrons in (3) states (local O 2p states) jump to the CB, generating the 340 nm excitation peak, while electrons jumping from (3) to (4) (local W 5d states) produce the 378 nm weak excitation band. Therefore, the 340 nm peak intensifies gradually with increasing La_{Y2} numbers (not more than Y2 sites numbers). When the doping concentration increases, the content variation of La_{Y3} is larger than those of La_{Y2} . The electrons in (5) also jump to the CB corresponding to 340 nm excitation. However, the transition from (5) to (6) becomes a direct transition leading to strong 592 nm excitation, which weakens the electron transition for the contribution of 340 nm. Therefore, the 340 nm intensity becomes weak (does not disappear) in high-concentration La^{3+} -doped samples.

From a phenomenological viewpoint, the occupation number of Y2 site becomes higher but does not reach saturation, and La^{3+} tends to occupy the Y3 sites at high doping concentrations. Thus, the 340 nm band intensity strengthens at low La content and then weakens with further increasing doping concentration. In addition, a few La^{3+} ions enter into the Y1 site as shown in table 1, and the transitions between the VB and the local states (1) can produce some excitation peaks around 500 nm. When La^{3+} occupies different Y sites, along with the oxygen pair, the local crystal structure shows different changes such as bond length and electronic density. The W-O bond length was measured as shown in Table S3. Since the six W-O bond lengths are unequal, the average values are computed. The average bond length variations in models $\text{La}_{Y1} + \text{V}_{\text{O}(36)}$, $\text{La}_{Y2} + \text{V}_{\text{O}(24)}$, and $\text{La}_{Y3} + \text{V}_{\text{O}(14)}$ are 0.048, 0.026, and 0.045 Å, respectively. One can see that the bond lengths change relative to the pristine system in model $\text{La}_{Y2} + \text{V}_{\text{O}(24)}$ is the smallest, and thus smallest distortion promotes the 340 nm excitation intensity. For models $\text{La}_{Y1} + \text{V}_{\text{O}(36)}$ and $\text{La}_{Y2} + \text{V}_{\text{O}(24)}$, bigger distortions lead to other forbidden transitions becoming allowed transitions, thus weakening the 340 nm intensity. Different bond length variations result in different local state distributions in the band gap.

Table 3 lists the energy level positions of VB maximum (VBM), local states, and CB minimum (CBM). From Figure 6, Figure S5 and Table 3, one can see that the 340 nm excitation band weakens or disappears when La^{3+} enters into the Y3 or Y1 sites. Therefore, the first principle calculation explains the gradual death of the 340 nm excitation band and the emergence of many new peaks. Finally, the schematic oxygen vacancy forming process is plotted (Figure S6).

Conclusion. In the present paper, we study the concentration effect of isovalent La^{3+} doping on the photoluminescence of monoclinic

Y_2WO_6 . The incorporating of La^{3+} into the matrix favors the formation of single and coupled oxygen vacancies. At low doping concentration, La^{3+} prefers to occupy the Y2 (2f) site, while at high concentration, it mainly occupies the Y3 (4g) site. When La occupies the Y2 (2f) site, the local states caused by the oxygen vacancy pair locate just below the CBM and connect with the VBM. When La occupies the Y3 (4g) site, new local energy bands appear. As a result, besides the emission of the W-O group in the visible region, there appear new emission and excitation bands because of the mid-gap excitation using light longer than 320 nm. At low La^{3+} doping concentration, the 340 nm excitation band is substantially intensified, resulting in visible emission. A series of excitation bands in the visible region also appear, causing strong near-infrared emission. The abundant change of the excitation and emission spectra with the La doping is ascribed to the single and coupled oxygen vacancy change and the selective occupation of La to different Y sites. In our previous articles³⁴, the $\text{Y}_{1.98}\text{WO}_6:0.02\text{Sm}^{3+}$ phosphors can emit white light under 340 nm excitation. The luminescence is mainly originated from the tungstate group and Sm^{3+} emission. In this paper, La doping in monoclinic Y_2WO_6 greatly improves luminescence intensity under 340 nm excitation. Therefore, the strong white-light emission can be anticipated through co-doping the non-activated La^{3+} and luminous Re^{3+} (Sm^{3+} , Eu^{3+}) in self-activated Y_2WO_6 host under the near-violet irradiation.

Experiment and calculation details

Samples preparation and characterization. $\text{Y}_2\text{WO}_6:\text{xLa}^{3+}$ ($\text{x} = 0$ and $0.01 \sim 0.05$) powders were prepared through solid-state reaction. The detailed experiment steps and characterization methods were described previously^{34,40}. For La^{3+} -doped samples, the raw materials were added different amounts of La_2O_3 . The chemical state of the La element was examined by x-ray photoelectric spectra (XPS) using a Thermo-electron ESCALAB 250 spectrometer equipped with monochromatic Al X-ray source (1486.6 eV).

Calculation procedures. To determine formation energy and the electronic structure, we use VASP software to simulate the doping effect in periodic supercell structures⁶⁹. In the following, the La_{Y1} model was used as an example to illustrate the calculation steps. First, a unitcell was built, and then relaxed fully. Second, the relaxed unitcell was expanded to a $1 \times 2 \times 1$ supercell. For samples containing single or coupled oxygen vacancy, we constructed and fully optimized the $1 \times 2 \times 1$ supercell, where one La substituted for Y1 and O1 or O1 and O2 (six-type oxygen sites) atom(s) near the W atom neighboring La was removed. Third, the defect formation energy ($E_{\text{formation}}$) of all $\text{La}_{Yk} + \text{V}_{\text{O}(ij)}$ models were calculated. Finally, when the $E_{\text{formation}}$ of one model was closest to the average value of the fifteen models in every type of La_{Yk} , the DOS and energy band structure were computed. In order to overcome the bandgap underestimation drawback of density function theory (DFT) calculation, the generalized gradient approximation (GGA) + U method was applied in all calculations. Through a series of tests, the optimal U values for O, Y, La and W were found to be 4.5, 0.0, 0.0 and 9.9 eV⁴⁰.

- Zhu, Y. J. & Chen, F. Microwave-assisted Preparation of Inorganic Nanostructures in Liquid Phase. *Chem. Rev.* **114**, 6462–6555 (2014).



2. Allix, M. *et al.* Synthesis and Structure Determination of the High Temperature Form of La_2WO_6 . *Cryst. Growth. Des.* **11**, 5105–5112 (2011).
3. Bhat, S. S. M. *et al.* Photoluminescence Tuning of $\text{Na}_{1-x}\text{K}_x\text{NdW}_2\text{O}_8$ ($0.0 < x < 0.7$) Nanoparticles: Synthesis, Crystal Structure and Raman Study. *Phys. Chem. Chem. Phys.* **16**, 18772–18780 (2014).
4. Blasse, G. The Luminescence of Closed-shell Transition-metal Complexes. New Developments. *Structure and Bonding* **42**, 1–41 (1980).
5. Zhang, C. L. *et al.* Large-scale Synthesis and Photoluminescence of Cobalt Tungstate Nanowires. *Phys. Rev. B* **87**, 035416–1–035416–8 (2013).
6. Wang, L. L. *et al.* Luminescence Properties of Nano and Bulk ZnWO_4 and Their Charge Transfer Transition. *J. Mater. Chem. C* **2**, 4651–4658 (2013).
7. Zhang, C. M. & Lin, J. Defect-related Luminescent Materials: Synthesis, Emission Properties and Application. *Chem. Soc. Rev.* **41**, 7938–7961 (2012).
8. Singh, B. P. *et al.* Enhanced Photoluminescence in $\text{CaMoO}_4:\text{Eu}^{3+}$ by Gd^{3+} Codoping. *Dalton. Trans.* **43**, 4779–4789 (2014).
9. Stavale, F. *et al.* Luminescence Properties of Nitrogen-doped ZnO . *J. Phys. Chem. C* **118**, 13693–13696 (2014).
10. Santos, M. A. *et al.* The Role of Short-range Disorder in BaWO_4 Crystals in the Intense Green Photoluminescence. *J. Phys. Chem. C* **115**, 12180–12186 (2011).
11. Boyle, T. J. *et al.* Synthesis and Characterization of Solvothermal Processed Calcium Tungstate Nanomaterials From Alkoxide Precursors. *Chem. Mater.* **26**, 965–975 (2014).
12. Li, H. Y. *et al.* Crystals Structure, Electronic Structure and Optical and Photoluminescence Properties of Eu(III) Ion-doped $\text{Lu}_6\text{Mo(W)O}_{12}$. *Inorg. Chem.* **50**, 12522–12530 (2011).
13. Bessiere, A. *et al.* Role of Crystal Defects in Red Long-lasting Phosphorescence of $\text{CaMgSi}_2\text{O}_6:\text{Mn}$ Diopsides. *J. Mater. Chem.* **22**, 19039–19046 (2012).
14. Huang, K. W. *et al.* Controlling the Activator Site to Tune Europium Valence in Oxyluoride Phosphors. *Chem. Mater.* **24**, 2220–2227 (2012).
15. Singh, M. B. P., Singh, J. & Singh, R. A. Luminescence Properties of Eu^{3+} -activated SrWO_4 Nanophosphors Concentration and Annealing Effect. *RSC. Adv.* **4**, 32605–32621 (2014).
16. Xia, Z. G. *et al.* Linear Structural Evolution Induced Tunable Photoluminescence in Clinopyroxene Solid-solution phosphors. *Sci. Rep.* **3**, 3310–1–3310–6 (2013).
17. Peng, Y. P. *et al.* The Effect of La_2O_3 in Tm^{3+} -doped Germanate-tellurite Glasses for $\sim 2 \mu\text{m}$ Emission. *Sci. Rep.* **4**, 5256–1–5256–5 (2014).
18. Lorbeer, C. *et al.* Charge Compensation in Re^{3+} ($\text{Re} = \text{Eu, Gd}$) and M^+ ($\text{M} = \text{Li, Na, K}$) Co-doped Alkaline Earth Nanofluorides Obtained by microwave Reaction With Reactive Ionic liquids Leading to Improved Optical Properties. *J. Mater. Chem. C* **2**, 9439–9405 (2014).
19. Weber, A. S., Grady, A. M. & Koodali, R. T. Lanthanide Modified Semiconductor Photocatalysts. *Catal. Sci. Technol.* **2**, 683–693 (2012).
20. Li, Q. H. *et al.* The Effect of Ca-substitution in La-site on the Magnetic Properties of $\text{La}_2\text{CoMnO}_6$. *J. Appl. Phys.* **116**, 033905–1–033905–4 (2014).
21. Morozov, V. A. *et al.* Incommensurate Modulation and Luminescence in the $\text{CaGd}_{2(1-x)}\text{Eu}_{2x}(\text{MoO}_4)_{4(1-y)}$ ($0 \leq x \leq 1, 0 \leq y \leq 1$) Red Phosphors. *Chem. Mater.* **25**, 4387–4396 (2013).
22. Arin, J. P. *et al.* Synthesis, Characterization and Optical activity of La-doped ZnWO_4 Nanorods by Hydrothermal Method. *Superlattice & Microsc.* **67**, 197–206 (2014).
23. Zhou, Y., Yan, B. & He, X. H. Controlled Synthesis and Up/Down-conversion Luminescence of Self-assembled Hierarchical architectures of Monoclinic $\text{AgRe}(\text{WO}_4)_2:\text{Ln}^{3+}$ ($\text{Re} = \text{Y, La, Gd, Lu}$; $\text{Ln} = \text{Eu, Tb, Sm, Dy, Yb/Er, Yb/Tm}$). *J. Mater. Chem. C* **2**, 848–855 (2014).
24. Sharma, K. G. & Singh, N. R. Synthesis and Luminescence Properties of $\text{CaMoO}_4:\text{Dy}^{3+}$ ($\text{M} = \text{W, Mo}$) Nanoparticles prepared via an Ethylene Glycol Route. *New J. Chem.* **37**, 2784–2791 (2013).
25. Fabeni, P. *et al.* Luminescence and Photo-thermally Stimulated Defects Creation Processes in PbWO_4 Crystals Doped With Trivalent Rare-earth Ions. *J. Lumin.* **136**, 42–50 (2013).
26. Nikl, M. *et al.* Decay Kinetics and Thermoluminescence of $\text{PbWO}_4:\text{La}^{3+}$. *Appl. Phys. Lett.* **71**, 3755–3757 (1997).
27. Chen, T. *et al.* First-principles Study on the La^{3+} Doping PbWO_4 Crystals for Different Doping Concentration. *Phys. Lett. A* **363**, 477–481 (2007).
28. Lv, W. C. *et al.* White Up-conversion Luminescence in Rare-earth-ion-doped YAlO_3 Nanocrystals. *J. Phys. Chem. C* **112**, 15071–15074 (2008).
29. Stankic, S. *et al.* Novel Optical Surface Properties of Ca^{2+} -doped MgO Nanocrystals. *Nano. Lett.* **5**, 1889–1893 (2005).
30. Kaczmarek, A. M. & Deun, R. V. Rare Earth Tungstate and Molybdate Compounds-From 0D to 3D Architectures. *Chem. Soc. Rev.* **42**, 8835–8848 (2013).
31. Chen, F. M. & Liu, X. H. Structure and Photoluminescence Properties of $\text{La}_2\text{Mo}(\text{WO}_6)_2:\text{Eu}^{3+}$ as Red Phosphors for White LED Application. *Opt. Mater.* **35**, 2716–2720 (2013).
32. Zhang, Z. J. Structure refinement of Lu_2WO_6 and luminescent Properties of Eu^{3+} , Pr^{3+} doped Lu_2WO_6 . *J. Alloy Compd.* **466**, 258–263 (2008).
33. Guzik, M. *et al.* Structural and Spectroscopic Characterization of Two Promising Nd-doped monoclinic or Tetragonal Laser Tungstates. *J. Mater. Chem.* **22**, 14896–14906 (2012).
34. Qian, H. J., Zhang, J. Y. & Yin, L. Q. Crystal Structure and Optical Properties of White Light Emitting $\text{Y}_2\text{WO}_6:\text{Sm}^{3+}$ Phosphors With Excellent Color Rendering. *RSC. Adv.* **3**, 9029–9034 (2013).
35. Wang, J. *et al.* Luminescent Metastable $\text{Y}_2\text{WO}_6:\text{Ln}^{3+}$ ($\text{Ln} = \text{Eu, Er, Sm, and Dy}$) Microspheres with Controllable Morphology via Self-assembly. *J. Mater. Chem.* **20**, 10894–10900 (2010).
36. Wang, Q. *et al.* Multicolor Bright Ln^{3+} ($\text{Ln} = \text{Eu, Dy, Sm}$) Activated Tungstate Phosphor for Multifunctional Applications. *Opt. Mater. Express.* **4**, 142–154 (2014).
37. Huang, M. N., Ma, Y. Y., Xiao, F. & Zhang, Q. Y. Bi^{3+} Sensitized $\text{Y}_2\text{WO}_6:\text{Ln}^{3+}$ ($\text{Ln} = \text{Dy, Eu, Sm}$) Phosphors for Solar Spectral Conversion. *Spectrochim. Acta. A* **120**, 55–59 (2014).
38. Blasse, G. & Dirksen, G. The Luminescence of Bismuth Tungstates. *Chem. Phys. Lett.* **85**, 150–152 (1982).
39. Noort, H. M. V. & Popma, T. J. A. Concentration-dependent Site Occupancy in Europium Doped Y_2WO_6 as studied by ^{151}Eu Mossbauer Spectroscopy. *Solid. State. Commun.* **55**, 77–79 (1985).
40. Ding, B. F., Qian, H. J., Han, C., Zhang, J. Y., Lindquist, S. E. & Wei, B. Oxygen Vacancy Effect on Photoluminescence Properties of Self-Activated Yttrium Tungstate. *J. Phys. Chem. C* **118**, 25633–25642 (2014).
41. Efremov, V. A., Tyulin, A. V., Trunov, V. K., Kudin, O. V., Yanovskii, V. K. & Voronkova, V. I. The Crystal-structure of Monoclinic Y_2WO_6 and Yb_2WO_6 . *Kristallografiya* **29**, 904–909 (1984).
42. Shannon, R. D. Revised Effective Ionic Radii and Systematic Studies of Interatomic Distances in Halides and Chalcogenides. *Acta. Cryst.* **A32**, 751–767 (1976).
43. Larson, A. C. & Dreele, R. B. V. General Structure Analysis System [Larson, A. C., Dreele, R. B. V. (ed.)] (Los Alamos National Laboratory Report LAUR 86-748, Cambridge, 2004).
44. Vanderdoesdebye, J. A. W. *et al.* Luminescence of $\text{Y}_{2(1-x)}\text{Eu}_{2x}\text{WO}_6$. *J. Lumin.* **43**, 339–353 (1989).
45. Lin, Q. P., Bu, X. H. & Feng, P. Y. An Infinite Square Lattice of Super-supertetrahedral T_6 -like Tin Oxyselelide Clusters. *Chem. Commun.* **50**, 4044–4046 (2014).
46. Vanderdoesdebye, J. A. W. *et al.* A Non-continuum Model for Energy Transfer in Europium-activated Oxytungstates. *J. Lumin.* **18/19**, 285–288 (1979).
47. Blasse, G. *et al.* The Luminescence of Uranium-activated Yttrium Tungstate. *J. Solid. State. Chem.* **21**, 99–103 (1977).
48. Mu, Z. F. *et al.* A Single-phase, Color-tunable, Broadband-excited White Light-emitting Phosphors $\text{Y}_2\text{WO}_6:\text{Sm}^{3+}$. *J. Lumin.* **146**, 33–36 (2014).
49. Kaczmarek, A. M., Heck, K. V. & Deun, R. V. Enhanced Luminescence in Ln^{3+} -doped Y_2WO_6 (Sm, Eu, Dy) 3D Microstructures through Gd^{3+} Codoping. *Inorg. Chem.* **53**, 9498–9508 (2014).
50. Blasse, G. & Grabmaier, B. C. Luminescence Materials [Blasse, G., Grabmaier, B. C. (ed.)] (Springer-Verlag, Berlin, 1994).
51. Zeng, H. B. *et al.* Blue Luminescence of ZnO Nanoparticles Based On Non-equilibrium Process: Defect Origin and Emission Controls. *Adv. Funct. Mater.* **20**, 561–572 (2010).
52. Li, Y. Z. *et al.* Investigation of Oxygen Vacancy and Photoluminescence in Calcium Tungstate Nanophosphors With Different Particle Sizes. *Mater. Res. Bull.* **50**, 36–41 (2014).
53. Wang, L. L. *et al.* Energy Transfer From Bi^{3+} to Eu^{3+} Triggers Exceptional Long-wavelength Excitation Band in $\text{ZnWO}_4:\text{Bi}^{3+}$, Eu^{3+} Phosphors. *J. Mater. Chem. C* **1**, 8033–8040 (2013).
54. William, G. F. & Francis, R. D. Infrared and Raman Selection Rules for Molecular and Lattice Vibration: the Correlation Method [William, G. F., Francis, R. D. (ed.)] (Wiley Inter Science, 1972).
55. Cavalcante, L. S. *et al.* A Combined Theoretical and Experimental Study of Electronic Structure and Optical properties of $\beta\text{-ZnMoO}_4$ Microcrystals. *Polyhedron* **54**, 13–25 (2013).
56. Blasse, G. & Corsmit, A. F. Electronic and Vibrational Spectra of Ordered Perovskites. *J. Solid. State. Chem.* **6**, 513–518 (1973).
57. Bode, J. H. G. *et al.* Vibrational Spectra of Compounds Ln_2MoO_6 and Ln_2WO_6 . *J. Solid. State. Chem.* **8**, 114–119 (1973).
58. Wagner, C. D. *et al.* Handbook of X-ray Photoelectron Spectroscopy [Wagner, C. D., Riggs, W. M., Davis, L. E., Moulder, J. F. (ed.)] (Eden Prairie, Minnesots 55344 1979).
59. Vasquez, R. P. X-ray Photoemission Measurements of $\text{La}_{1-x}\text{Ca}_x\text{CoO}_3$ ($x = 0, 0.5$). *Phys. Rev. B* **54**, 14938–14941 (1996).
60. Chen, J. T. *et al.* The Effect of La Doping Concentration on the Properties of Zinc Oxide Films Prepared by the Sol-gel Method. *J. Cryst. Growth.* **310**, 2627–2632 (2008).
61. Beyreuther, E., Grafstron, S. & Eng, L. M. XPS Investigation of Mn Valence in Lanthanum Manganite Thin Films Under Variation of Oxygen Content. *Phys. Rev. B* **73**, 155425–1–155425–9 (2006).
62. Longo, V. M. *et al.* Hierarchical Assembly of CaMoO_4 Nano-octahedrons and Their Photoluminescence Properties. *J. Phys. Chem. C* **115**, 5207–5219 (2011).
63. Magraso, A. & Haugsrud, R. Effects of the La/W Ratio and Doping on the Structure, Defect Structure, Stability and Functional Properties of Proton-conducting Lanthanum Tungstate $\text{La}_{28-x}\text{W}_{4+x}\text{O}_{54+\delta}$. A Review. *J. Mater. Chem. A* **2**, 12630–12641 (2014).
64. Santos, M. A. *et al.* Contribution of Structural Order-Disorder to the Green Photoluminescence of PbWO_4 . *Phys. Rev. B* **75**, 165105–165105–11 (2007).



65. Soni, A. K. & Rai, V. K. Intrinsic Optical Bistability and Frequency Upconversion in Tm^{3+} - Yb^{3+} -Codoped Y_2WO_6 Phosphor. *Dalton. Trans.* **43**, 13563–13570 (2014).
66. Cavalcante, L. S. *et al.* Electronic Structure, Growth Mechanism and Photoluminescence of CaWO_4 Crystals. *Cryst. Eng. Comm.* **14**, 853–868 (2012).
67. Liang, Y. *et al.* ZnMoO_4 Micro- and Nanostructures Synthesized by Electrochemistry Assisted laser Ablation in Liquids and Their Optical properties. *Cryst. Growth. Des.* **12**, 4487–4493 (2012).
68. Huang, J. P. *et al.* Determining the Structure of Tetragonal Y_2WO_6 and the Site Occupation of Eu^{3+} dopant. *J Solid. State. Chem.* **184**, 843–847 (2011).
69. Kresse, G. & Furthmuller, J. Efficient Iterative Schemes for Ab Initio Total-Energy Calculations Using a Plane-Wave Basis Set. *Phys. Rev. B.* **54**, 11169–11186 (1996).

Acknowledgments

This project was financially supported by the National Science Foundation of China under Grant (No. 91222110 and 51472013), the PhD Programs Foundation of the Ministry of Education of China under Grant No. 20121102110027, State Key Laboratory of New Ceramic and Fine Processing Tsinghua University (No. KF201414) and the high-performance computing platform of Network Information Center in Beihang University.

Author contributions

B.F.D. completed the writing of the manuscript and first-principle calculation. C.H. performed the sample preparation and all the experimental tests. L.R.Z. fitted the data of synchrotron radiation. J.Y.Z. designed the whole research and revised the articles. R.M.W. and Z.L.T. participated in the discussion of the data and proposed many good suggestions.

Additional information

Supplementary information accompanies this paper at <http://www.nature.com/scientificreports>

Competing financial interests: The authors declare no competing financial interests.

How to cite this article: Ding, B. *et al.* Tuning oxygen vacancy photoluminescence in monoclinic Y_2WO_6 by selectively occupying yttrium sites using lanthanum. *Sci. Rep.* **5**, 9443; DOI:10.1038/srep09443 (2015).



This work is licensed under a Creative Commons Attribution 4.0 International License. The images or other third party material in this article are included in the article's Creative Commons license, unless indicated otherwise in the credit line; if the material is not included under the Creative Commons license, users will need to obtain permission from the license holder in order to reproduce the material. To view a copy of this license, visit <http://creativecommons.org/licenses/by/4.0/>